

# The Chromospheric Telescope

C. Bethge<sup>1,2</sup>, H. Peter<sup>3,1</sup>, T. J. Kentischer<sup>1</sup>, C. Halbgebachs<sup>1</sup>, D. F. Elmore<sup>4</sup>, and C. Beck<sup>5</sup>

<sup>1</sup> Kiepenheuer-Institut für Sonnenphysik, Schöneckstr. 6, 79104 Freiburg, Germany  
e-mail: bethge@ucar.edu

<sup>2</sup> High Altitude Observatory, National Center for Atmospheric Research\*, PO Box 3000, Boulder, CO 80307, USA

<sup>3</sup> Max-Planck-Institut für Sonnensystemforschung, 37191 Katlenburg-Lindau, Germany

<sup>4</sup> National Solar Observatory, 3010 Coronal Loop, Sunspot, NM 88349, USA

<sup>5</sup> Instituto de Astrofísica de Canarias (CSIC), via Lactea, 38205 La Laguna, Tenerife, Spain

Received 9 June 2011 / Accepted 27 July 2011

## ABSTRACT

**Aims.** We introduce the *Chromospheric Telescope* (ChroTel) at the Observatorio del Teide in Izaña on Tenerife as a new multi-wavelength imaging telescope for full-disk synoptic observations of the solar chromosphere. We describe the design of the instrument and summarize its performance during the first one and a half years of operation. We present a method to derive line-of-sight velocity maps of the full solar disk from filtergrams taken in and near the He I infrared line at 10 830 Å.

**Methods.** ChroTel observations are conducted using Lyot-type filters for the chromospheric lines of Ca II K, H $\alpha$ , and He I 10 830 Å. The instrument operates autonomically and gathers imaging data in all three channels with a cadence of down to one minute. The use of a tunable filter for the He I line allows us to determine line-shifts by calibrating the line-of-sight velocity maps derived from the filtergram intensities with spectrographic data from the Tenerife Infrared Polarimeter at high spatial and spectral resolution.

**Results.** The robotic operation and automated data reduction have proven to operate reliably in the first one and half years. The achieved spatial resolution of the data is close to the theoretical limit of 2 arcsec in H $\alpha$  and Ca II K and 3 arcsec in He I. Line-of-sight velocities in He I can be determined with a precision of better than 3–4 km s<sup>-1</sup> when co-temporal spectrographic maps are available for calibration.

**Conclusions.** ChroTel offers a unique combination of imaging in the most important chromospheric lines, along with the possibility to determine line-of-sight velocities in one of the lines. This is of interest for scientific investigations of large-scale structures in the solar chromosphere, as well as for context imaging of high-resolution solar observations.

**Key words.** Sun: chromosphere – telescopes

## 1. Introduction

Full-disk observations of the Sun, from both the ground and space, have always played an important role in solar physics because they are not only essential to global solar studies, e.g., for helioseismology and solar activity, but also provide contextual information for observations at high resolution that study only small parts of the solar disk. Among the most prominent examples are the GONG network (Harvey et al. 1996) and the MDI instrument onboard SOHO (Scherrer et al. 1995). It is widely believed that key insight emerges predominantly from high-resolution observations advancing to smaller and smaller structures in the Sun's atmosphere. Ground-based full-disk instruments commonly share the disadvantage of a comparably low spatial resolution. They must be operated seeing-limited because adaptive optics can correct only for a small portion of the solar disk. However, despite this disadvantage, they are still vital in solar research – first and foremost for structures on larger scales up to the complete disk, but also for rarely occurring events that are often missed when examining only a small fraction of the disk. Here, we present such an instrument for observations of the solar chromosphere.

Chromospheric full-disk observations are often performed in the spectral lines of Ca II K (3933.7 Å) and H $\alpha$  (6562.8 Å) because both lines are known to indicate the presence and the structure of magnetic fields. Prominent examples include the RISE-PSPT instruments observing in Ca II K (Ermolli et al. 1998) at the Osservatorio Astronomico di Roma (OAR) and the Mauna Loa Solar Observatory (MLSO), as well as the H $\alpha$  patrol instrument of the Kanzelhöhe Observatory (Otruba 1999) in Austria, which is part of the global H $\alpha$  network (Steinberger et al. 2000).

The He I triplet at 10 830 Å has become an increasingly popular diagnostic of the chromosphere, although its formation process is complicated. In spectropolarimetry, this is due to the sensitivity of the polarization signal to both the Hanle and the Zeeman effect, rendering the line(s) an ideal tool for both strong and weak magnetic field regions (e.g., Rüedi et al. 1995; Trujillo Bueno et al. 2005). However, it is also very useful for full-disk observations because the line is formed entirely in the upper chromosphere (that is at chromospheric temperatures) or the lower transition region with no photospheric contributions. In addition, the line formation is strongly influenced by coronal emission because the triplet states are mainly populated by the photoionization-recombination mechanism (Centeno et al. 2008). This permits an estimation of coronal activity in ground-based observations – coronal holes for example are clearly

\* The National Center for Atmospheric Research is sponsored by the National Science Foundation.

visible in He I 10 830 Å (see e.g., Dupree et al. 1996). However, observations can still suffer from photospheric contamination in regions with little photospheric activity and/or very low coronal illumination because the line becomes so optically thin that the photospheric continuum shines through.

Telescopes observing in He I are CHIP (Elmore et al. 1998) at MLSO and the OSPAN instrument (formerly ISOON, see Neidig et al. 1998) at the National Solar Observatory at Sacramento Peak. The latter also provides observations in H $\alpha$ .

The Chromospheric Telescope *ChroTel* introduced here records data in all three spectral lines (Ca II K, H $\alpha$ , He I 10 830 Å) with a cadence as fast as one minute. This is done almost simultaneously, and as the different lines sample different temperature regimes (and therefore heights), this gives a more holistic view of phenomena in the chromosphere and their connection to higher layers. In addition, the data in He I are taken at seven wavelength positions in and around the He I triplet with a tunable Lyot-type filter. As we later demonstrate, the line-of-sight (LOS) velocities across the full disk can be determined with these filtergrams, which is essential for investigating the dynamics in the chromosphere. Since it is located on Tenerife, i.e., in a different time-zone from both the CHIP and OSPAN instruments, *ChroTel* will also increase the available temporal coverage of full-disk data in He I 10 830 Å.

The outline of the paper is as follows. Section 2 gives a brief overview of the scientific scope of *ChroTel*, followed by a description of the instrument and data in Sects. 3 and 4. Section 5 illustrates our method for extracting information about line-shifts from the intensity filtergrams in He I. Finally, we make some concluding remarks on the data quality and the potential of the method for the velocity determination.

## 2. Scientific scope

*ChroTel* observes a wide range of solar phenomena of scientific importance, some of which are presented here. This is of course neither complete nor representative of what can be achieved with the data, but gives an impression of the potential of the instrument.

### 2.1. Filaments, flares, and Moreton waves

Filaments (and prominences) are naturally a subject of chromospheric full-disk observations both for statistical reasons and because they often occupy a significant fraction of the solar disk. The measurement of their LOS velocities permits the examination of large-scale flows within filaments. Along with information about the magnetic field configuration, this can serve as an important ingredient of filament models, especially for the onset of flares and coronal mass ejections (CMEs).

Related to this are Moreton waves (Moreton & Ramsey 1960), which are horizontal waves traditionally observed in H $\alpha$  that propagate away from flare sites at speeds of up to 2000 km s<sup>-1</sup>. Authors have tried to establish connections between EIT waves (the name stems from observations of the waves with the Extreme ultraviolet Imaging Telescope, see Thompson et al. 1998) higher up in the atmosphere and Moreton waves, primarily on the basis of the co-spatiality of the two phenomena. While some authors indeed find co-spatial features (e.g., Thompson et al. 2000; Warmuth et al. 2002), others come to a different result (e.g., Eto et al. 2002; Okamoto et al. 2004) and question whether a connection exists.

Investigations of observations in an intermediate layer seem favorable and have indeed been done with data in He I 10 830 Å. Vršnak et al. (2002) find co-spatiality in H $\alpha$ , He I, and EIT maps, with a forerunner in He I with respect to H $\alpha$ . They conclude that the waves are of a mechanical nature, whereas Gilbert et al. (2004) suggest that the co-spatial features they find in He I with respect to EIT data indicate a “chromospheric imprint” of a wave in the corona triggered by the enhanced coronal EUV emission, which then again leads to an increase in the He I absorption. With almost co-temporal data in both H $\alpha$  and He I, this controversy can be investigated using *ChroTel* data. As Gilbert et al. (2004) conclude in their paper: “In any case, a high-time cadence He I 10 830 data set should provide an additional useful tool in the study of coronal waves.”

The cadence of 3 min for the synoptic observations is, however, not perfectly suited to investigating short-lived events such as flares or waves travelling at speeds of up to 2000 km s<sup>-1</sup>. This would have to be done in a dedicated mode of operation looking for these events, e.g., by taking images with a high cadence only in the line cores of H $\alpha$  and He I. Since Moreton waves travel a significant distance during the acquisition time of about 8 s for the whole He I filtergram sequence, the determination of LOS velocities in He I is of limited use for this purpose, but the propagation of the waves can also be traced in high-cadence intensity images, e.g., using the differences between consecutive images.

### 2.2. Supersonic downflows

Magnetic flux in the quiet Sun appears in two different shapes: diffuse and weak magnetic flux in the internetwork, and concentrated magnetic field in both the network and isolated flux tubes. A possible method for the transition from the diffuse to the concentrated state was proposed by Parker (1978), which he called the *superadiabatic effect*: when the magnetic field lines are shuffled to and “squeezed” at the boundaries of supergranules, the magnetic field strength rises and suppresses convection. In these regions, this leads to a cooling of the plasma which is already in a general downdraft region. The downdraft is further enhanced by the cooling, through which plasma in the upper parts of a filled flux tube can lose its support from below and the flux tube becomes evacuated rapidly. The plasma from above should then (nearly) undergo a free-fall motion in this picture, which is usually referred to as *convective collapse*. These motions indeed were observed in a plage region by Schmidt et al. (2000) in H $\beta$  and He I 10 830 Å, with plasma movements at a constant acceleration of 200 m s<sup>-2</sup>. The motions lasted for about 90 s, which agrees with the results of Grossmann-Doerth et al. (1998) who inferred a duration of several minutes for convective collapses from 2D simulations. It is puzzling, however, that the reports of these events are very sparse, although Parker’s scenario should be rather general and occur essentially on an everyday basis for the Sun.

Lagg et al. (2007) also report high-velocity downflows in He I, but in the vicinity of a growing pore. The downflows were lasting (and increasing) for over an hour, so the convective collapse scenario in this case is rather unlikely. The authors interpreted their results as a continuous drainage of a slowly rising magnetic flux tube, leading to increasing downflows in the footpoints of the loop.

With *ChroTel*, it will be possible to improve the quality of the statistics of the rates and properties of these events. The downflows in the aforementioned observations were seen in regions extending from about 5 to 30 arcsec, with velocities up to

42 km s<sup>-1</sup>. In Sect. 5, we demonstrate that this should be easily accessible with ChroTel data in He I.

### 2.3. Onset of the fast solar wind in the chromosphere?

It has been known for many decades that the solar wind exhibits a slow and a fast component, the latter having average speeds of 700–800 km s<sup>-1</sup> (e.g. Phillips et al. 1995). It is also known that the fast component emerges from coronal holes (e.g., Krieger et al. 1973), i.e., regions appearing darker than their surroundings at EUV and X-ray wavelengths, although there are indications that it might also emerge from quiet Sun regions (Habbal et al. 1997).

It is still unclear, however, at which height and temperature the acceleration of the fast solar wind sets in. Dupree et al. (1996) investigated wing asymmetries in He I 10 830 Å profiles, i.e., in the upper chromosphere and lower transition region, from scans covering two polar coronal holes. The profiles in the coronal holes were found to be blueshifted, with a center-to-limb variation indicating a line-of-sight effect for the velocities, i.e., the amplitudes of the velocities were found to be dependent on the cosine of the heliocentric angle. This was interpreted as a radial outflow in the coronal holes and as the onset of the fast solar wind at chromospheric heights.

Tu et al. (2005) investigated SUMER (Wilhelm et al. 1995) scans of a polar coronal hole in the emission lines of Si II, C IV, and Ne VIII. The Ne VIII emission forming in the lower corona at 6 × 10<sup>5</sup> K was found to be blueshifted on average by 9 km s<sup>-1</sup>, whereas in the C IV emission that is formed at 1 × 10<sup>5</sup> K, only weak signatures of outflows were seen at the disk center (Dere et al. 1989) and at the poles (Peter 1999; Peter & Judge 1999). The question of course arises of how the blueshifts in He I 10 830 Å can depict the onset of the fast solar wind when only weak outflows are seen in C IV higher up in the atmosphere.

Along with co-temporal velocity information about the transition region, ChroTel can help us to determine whether the outflows seen by Dupree et al. (1996) are indeed a signature of the fast solar wind in the chromosphere or should be interpreted in a different way. As we show in Sect. 5, coronal holes pose a challenge to the velocity determination with ChroTel filtergrams because the intrinsic He I absorption is very weak in these regions. However, this might be addressed with the averaging of data because coronal holes are long-lived phenomena.

## 3. The instrument

The configuration of the instrument is described in detail in Kentischer et al. (2008) and Halbgewachs et al. (2008), so only a brief overview is given here.

### 3.1. Technical design and guiding

The outdoor structure of the telescope is a domeless turret in an alt-azimuth mount. The turret is sealed to protect the optical elements from wind, humidity, and extreme temperatures. Figure 1a shows the telescope structure attached to the building of the Vacuum Tower Telescope (VTT) on Tenerife.

Because of the alt-azimuth mount both the azimuth and the elevation axis have to be rotated in order to follow the position of the Sun during the day. The guiding is conducted in three consecutive steps. First, the values for azimuth and elevation of the Sun on the sky are calculated from ephemerides, not taking into account atmospheric refraction. Second, a position-sensing

detector (PSD) corrects small and slowly varying deviations of the Sun's designated position within a field-of-view (FOV) of 2.2°. The last step is the compensation of fast image movements with a tip-tilt mirror (M5 in Fig. 1b). It operates with a closed control loop at a cycle time of 108 μs and within a FOV of 0.7°. The pointing accuracy of this system is better than 0.5 arcsec.

### 3.2. Optics

The light enters through a wedged and anti-reflection-coated entrance window (W1). The window is protected by a shutter when the instrument is not operating to minimize contaminations by dust and humidity. The light is redirected to the optics lab inside the VTT building by the flat telescope mirrors M1-3 and imaged onto a single CCD by a combination of achromatic lenses (L1:  $f = 2250$  mm, 100 mm aperture; L4:  $f = 800$  mm; L5:  $f = 600$  mm; L6:  $f = 500$  mm; L7:  $f = 800$  mm) and field lenses (L2-3). The aperture of 100 mm leads to a theoretical resolution limit of 1 arcsec for the calcium channel, 1.7 arcsec for H $\alpha$ , and 2.7 arcsec for He I. The spatial sampling on the 2048 × 2048 pixel CCD is about 1 arcsec per pixel, i.e., in the first two channels, the spatial resolution is sampling limited to about 2 arcsec by the detector.

All channels are recorded with one camera, hence the CCD must be sensitive over a large wavelength range from 393 nm to 1083 nm. A Kodak KAF-4320E CCD was selected, operated in a water-cooled Spectral Instruments Series 800 camera. The detector has a dynamic range of 14 bit, a pixel size of 24 × 24 μm, and a quantum efficiency (QE) of around 35% for Ca II K, 63% for H $\alpha$ , and 2% for He I.

To perform observations in all three spectral lines, the beam has to be redirected successively to three Lyot-type filters (see Sect. 3.3). For this, an in-house developed *filter exchange unit* (FEU) is used: the filters are mounted in an equilateral triangle setup with static flat mirrors both at the entrance and the exit of the filters (M8-9a,b,c in Fig. 1b). These mirrors are tilted by 45° with respect to the optical axis of the filters. Two rotatable mirrors (M7 and M10), also tilted by 45°, redirect the light to one of the static mirrors sets, hence through one of the Lyot filters. Rotating the (coupled) mirrors M7 and M10 by 120° around the axis coinciding with the direction of the incident light then allows a different filter to be selected. The mirrors M7-10 have a reflectivity of 90% at the relevant wavelengths, i.e., the FEU entails a loss of more than one-third of the incident intensity. Along with the low QE of the detector in the Ca II K and He I wavelengths, this involves comparably long exposure times of up to 1 s in these channels as shown in Table 1.

Flatfielding is done using a diffuser plate that can be inserted into the beam when necessary. The diffuser plate is custom-made and generates a uniform intensity over a larger angular range than regular holographic diffuser plates. It is mounted within the outside telescope structure to take care of contaminations on all subsequent imaging optics. The diffuser plate rotates during the flatfield exposures to compensate for possible inhomogeneities in the manufacturing process. To do this, the period of the rotation is chosen as an integer multiple of the exposure time. Flatfields are currently taken once per hour in every channel.

### 3.3. Lyot filters

For each of the spectral lines, a Lyot-type birefringent narrow-band filter is used for the observations. All filters contain

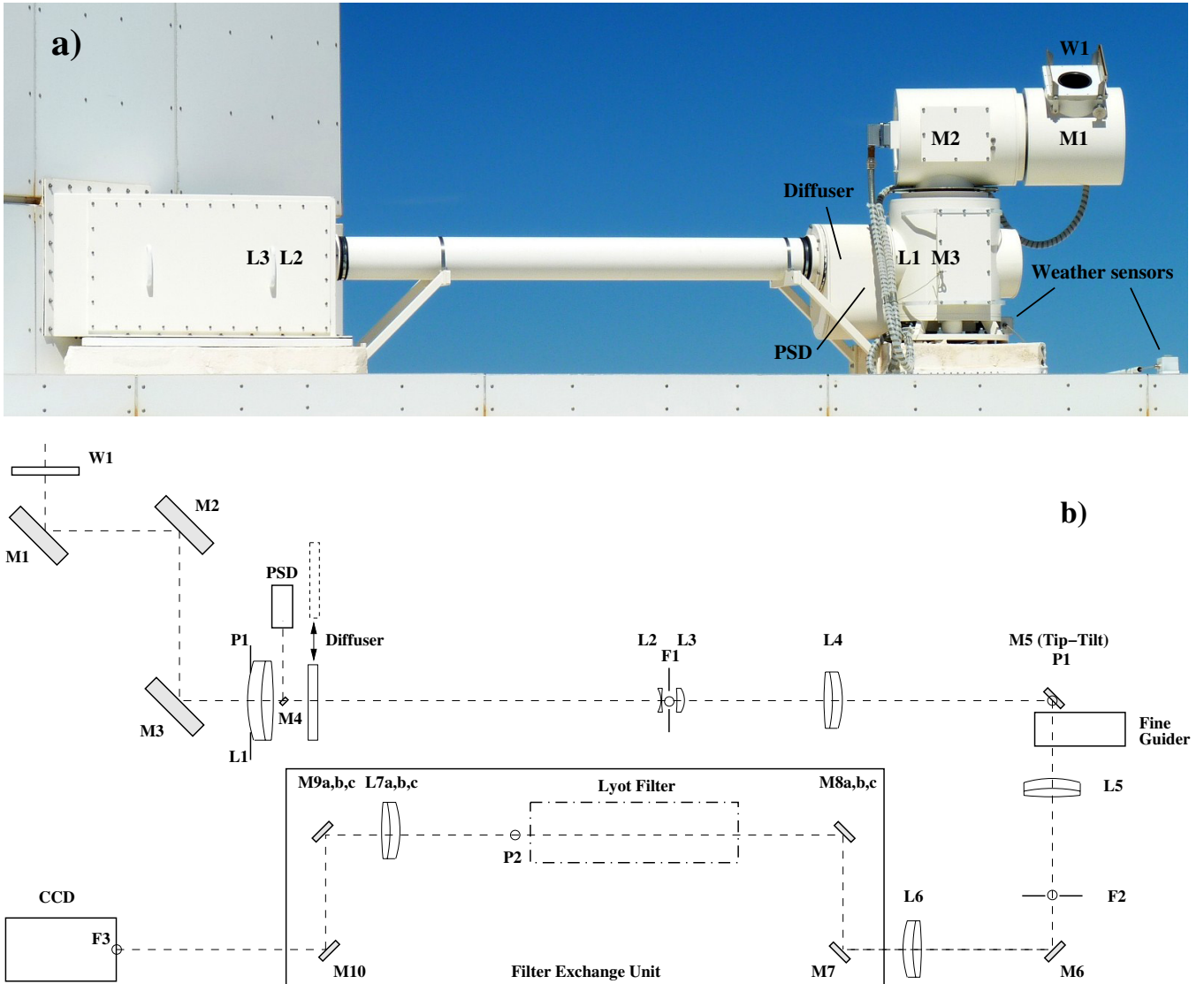


**Fig. 1.** **a)** Telescope structure outside the optical lab. **b)** Schematic overview of the optical path (not to scale): W1 entrance window, M1-3 telescope mirrors, L1 telescope lens with aperture, PSD position sensing detector, L2-3 field lenses, L4-7a,b,c achromatic lenses, M5 tip-tilt mirror, M7/M10 rotatable mirrors, M8-9a,b,c static mirrors, F1-3 focal planes, and P1-2 pupil planes.

**Table 1.** Overview of the observed spectral lines.

Spectral line	Wavelength [Å]	Lyot filter widths FWHM [Å]	Typical exposure time [ms]	Minimum cadence [s]	
				single channel	all channels
Ca II K	3933.7	<i>0.3</i> ; 0.6; 1.2	1000	10	60
H $\alpha$	6562.8	<i>0.5</i> ; 1.0	100	10	60
He I	10830.3	<i>1.3</i>	1000	30	60

**Notes.** The values in italics indicate the default settings for the synoptic observations.

wide-fielded elements for a larger monochromatic acceptance angle. We now provide a short description of each Lyot filter:

**Ca II K:** the wavelength of the filter passband is adjusted to the central minimum of the Ca II K line at 3933.7 Å. The FWHM of the filter passband in the narrowest possible mode is 0.3 Å, which is the default setting for the synoptic observations (see Table 1). This is broad enough to observe the emission of both the K<sub>2r</sub> and K<sub>2v</sub> emission peak up to about 0.25 Å on the red and blue side of core of the line. Detachable polarizers at the entrance

and the exit of the filter also allow filter passbands with a FWHM of 0.6 Å and 1.2 Å. Figure 2 shows a measurement from 2011 of the narrowest possible filter passband. The FWHM of the central transmission peak determined from a Gaussian fit to the curve is 0.29 Å. The measurement also revealed a slightly enhanced contribution from a side lobe in the red wing of the Ca II K line.

**H $\alpha$ :** the FWHM of the filter passband in the default setting is 0.5 Å. It can be widened to 1.0 Å when a detachable entrance polarizer is removed. An additional contrast element can be

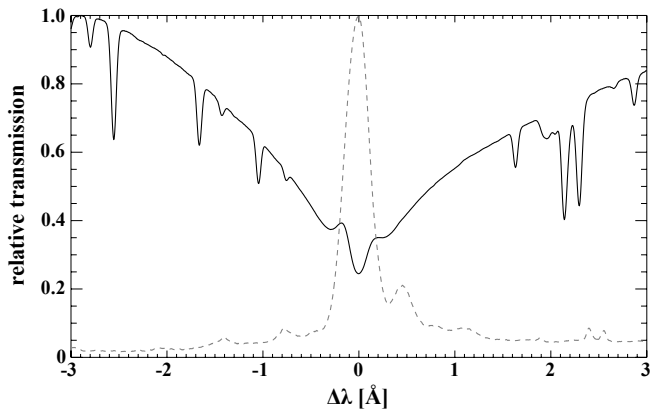


**Fig. 2.** Measured passband (grey dashed line) of the Lyot filter used for ChroTel Ca II K observations. The zero point marks the minimum of the Ca II K line at 3933.7 Å. For comparison, a spectrum around the Ca II K line is overplotted (solid line, recorded with the spectrograph of the VTT).

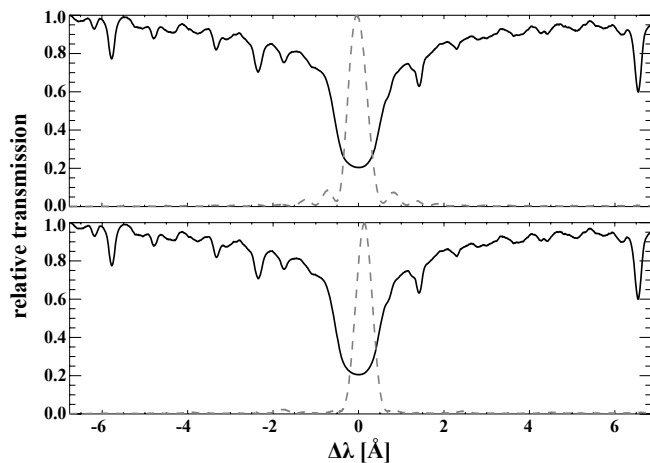


**Fig. 3.** Measured passbands (grey dashed lines) of the Lyot filter used for ChroTel H $\alpha$  observations. The zero point marks the minimum of the H $\alpha$  line at 6562.8 Å. *Top:* filter passband without contrast element. *Bottom:* filter passband with contrast element. For comparison, a spectrum around the H $\alpha$  line is overplotted (solid lines, recorded with the spectrograph of the Schauinsland Observatory).

used to suppress side lobes of the transmission curve. Figure 3 shows a measurement of the transmission curve from 2009 without and with the contrast element. In the latter case, the side lobes are significantly reduced, whereas the central wavelength of the transmission peak is shifted slightly towards the blue by 0.1 Å. This is nevertheless the preferable (and default) setting because the wings of the line are so bright compared to the core that the fraction of the intensity coming from the side lobes is over 70% when the contrast element is not used. With the contrast element, this drops to 40%, i.e., despite the shift, the largest fraction of the signal comes from the core of the line. The FWHM of the central transmission peak determined from a Gaussian fit is 0.48 Å.

He I 10 830 Å: A tunable filter is used for the observations in the He I infrared triplet. It was assembled by the High Altitude Observatory based on the design of the filter for the CHIP instrument (Elmore et al. 1998). The filter contains liquid crystal variable retarders (LCVR) between the birefringent stages, which allow a rapid adjustment of the central wavelength position of the transmission peak. CHIP acquires filtergrams in and around the

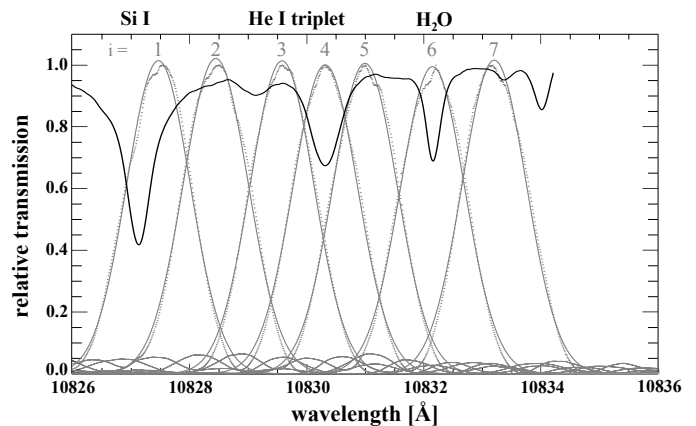


**Fig. 4.** Measured passbands of the tunable Lyot filter used for ChroTel He I 10 830 Å observations. *Grey dotted lines:* measured values. *Grey solid lines:* polynomial fit to the measurements. Central wavelength positions for the passbands in Ångstroms (Å), from left to right: 10 827.45, 10 828.47, 10 829.60, 10 830.30, 10 831.00, 10 832.13, 10 833.15. For comparison, a spectrum around the He I triplet from a plage region is overplotted in black (smoothed; observed with the Tenerife Infrared Polarimeter).

He I line at seven fixed wavelength positions in a non-equidistant order. These wavelengths were also chosen for ChroTel to ensure the comparability of the data of the two instruments. In Sect. 5, we show that these filtergrams can be used to determine line-shifts in He I 10 830 Å, hence chromospheric LOS velocities. Figure 4 shows a measurement of the seven transmission curves of the He I Lyot filter from 2006. The overplotted He I profile comes from a plage region. With its enhanced line depth, it shows a favorable case for the determination of velocities. In the quiet Sun, the line depth is substantially smaller than for the profile shown here.

The mean FWHM of the passbands obtained from polynomial fits to the data is 1.29 Å. Shifting the central wavelength position with the LCVRs is done in less than 60 ms, i.e., with a typical exposure time of 1000 ms, all filtergrams are obtained within less than 8 s.

## 4. Operation

ChroTel was designed as a monitoring instrument for synoptic observations. It operates autonomously and continuously, weather permitting, and can also be remote-controlled. The instrument starts operating automatically in the morning and shuts down in the evening, or in case of unsafe conditions, which are being recognized based on data from weather sensors for wind, humidity, and brightness. As soon as the conditions are safe again after the instrument has shut down, observations continue automatically.

All involved hardware components are controlled by a telescope control software written in LabView. The software allows one to initiate actions such as taking flatfields, choosing channels, and defining exposure times etc. within a text script. By default, a standard script is run for the regular operation described in Sect. 4.1. Other scripts can be used to customize the mode of operation, e.g., to coordinate observations with the nearby spectrograph at the VTT. Requests for specific modes of operation can be addressed to the Kiepenheuer Institute<sup>1</sup> (Freiburg,

<sup>1</sup> Send observation requests to: chrotel-inquiry@kis.uni-freiburg.de

**Table 2.** Overview of the data products from ChroTel.

Data type	Cadence [min]	Resolution [pixels]	Format	Availability
Scientific	3	2048 × 2048	FITS	Next day
Preview and live pictures	3	1024 × 1024	JPG	Few minutes after recording
Movies	3	512 × 512	AVI	Next day

Germany). While no limitations on observation requests are in effect at the moment, requests for high-cadence observations over extended periods of time might be denied or limited in order not to endanger the usefulness of the synoptic program.

#### 4.1. Synoptic observations

An image is acquired in each channel once every three minutes in the regular mode of operation. Small variations in the time consumed by computer communications limit the precision of the cadence within one channel to  $\pm 1$  s. Data in the three spectral lines cannot be recorded simultaneously because the single camera allows only for one channel at a time. This leads to a temporal offset of about 10–15 s between the channels.

Single-channel observations can be done upon request with a minimum cadence of 10 s in Ca II K and H $\alpha$  and 30 s in He I. The minimum cadence for observations in all three channels is one minute.

#### 4.2. Data reduction and availability

All data reduction, processing, and transfer is automatized. Every acquired image is instantly corrected for bias and gain with the most recent dark and flatfield exposures. In practice, this means that first the dark current is subtracted from both the flatfield and the observational data. All zero values in the flatfield are then subsequently replaced by unity to avoid a division by zero. A gain table is computed then from the flatfield, i.e., the pixel values are rescaled with a division by the median value to a range around unity to maintain the dynamic range of the observational data. As a last step, the observational data are divided by the gain table. The reduced data are then saved as 16-bit integer files in gzipped FITS format. As a byproduct, live images are created as 1024 × 1024 pixel JPG files, which are available a few minutes after recording on the website of the Kiepenheuer Institute. They are also used as a guiding aid for the nearby VTT and Gregor telescopes and later on as preview images for the data. Observations acquired 300 days per year and 7 h per day would generate a yearly amount of data of about 5 TB.

Overnight, the data are transferred from Tenerife to Freiburg to make them accessible for public use the next day. This includes the automated creation of daily overview movies and webpages for all channels. Table 2 gives an overview of the provided data products and the times they are available<sup>2</sup>.

<sup>2</sup> All data are open for scientific usage and can be accessed at the following addresses:

Live/most recent images:

<http://www.kis.uni-freiburg.de/index.php?id=457&L=1>

Anonymous ftp access:

<ftp://archive.kis.uni-freiburg.de/pub/chrotel/>

Overview of available data:

<http://www.kis.uni-freiburg.de/~chrotel/index.html>

#### 4.3. Instrument performance and data quality

The robotic operation and automatic data processing has proven to be reliable in the first one and a half years of operation. Any outages were caused mainly by bad weather, maintenance, or overall facility shutdowns in the winter.

Figure 5 presents some ChroTel full-disk images in all channels acquired on 31 August 2010. In addition, cutouts are shown to give a visual impression of the full spatial resolution of the images. The bottom row demonstrates that the smallest visible structures in H $\alpha$  and He I are close in size to the theoretical resolution limits of 2 arcsec in H $\alpha$  and 2.7 arcsec in He I. In Ca II K, the theoretical limit of 2 arcsec is not entirely achieved owing to the long exposure time that is necessary in this channel and the higher susceptibility to seeing at shorter wavelengths.

The mean spatial resolution of the data was computed for three sample days in summer 2010 (July 26, July 31, August 3). In a box of 800 × 800 pixels covering both quiet Sun and active regions, the Fourier power as a function of spatial frequency was determined. A flat part in this curve, i.e., when the Fourier power is the same for all frequencies, represents the Fourier transformation of white noise where no information is left in the data. The point where the curve becomes flat therefore marks the resolution limit. The determination of this point is not exact, but nevertheless gives a rough estimate of the spatial resolution of the data. For the data of the aforementioned three days, the mean spatial resolution in all channels turned out to be about two times worse than the theoretical resolution limit, i.e., the smallest resolved structures are about twice as large. This is predominantly caused by deteriorating seeing conditions in the afternoon.

For the same days, the mean scattered light at 1.1  $R_{\odot}$  was determined as 0.13 in Ca II K and 0.04 in both H $\alpha$  and He I relative to the mean intensity on the solar disk.

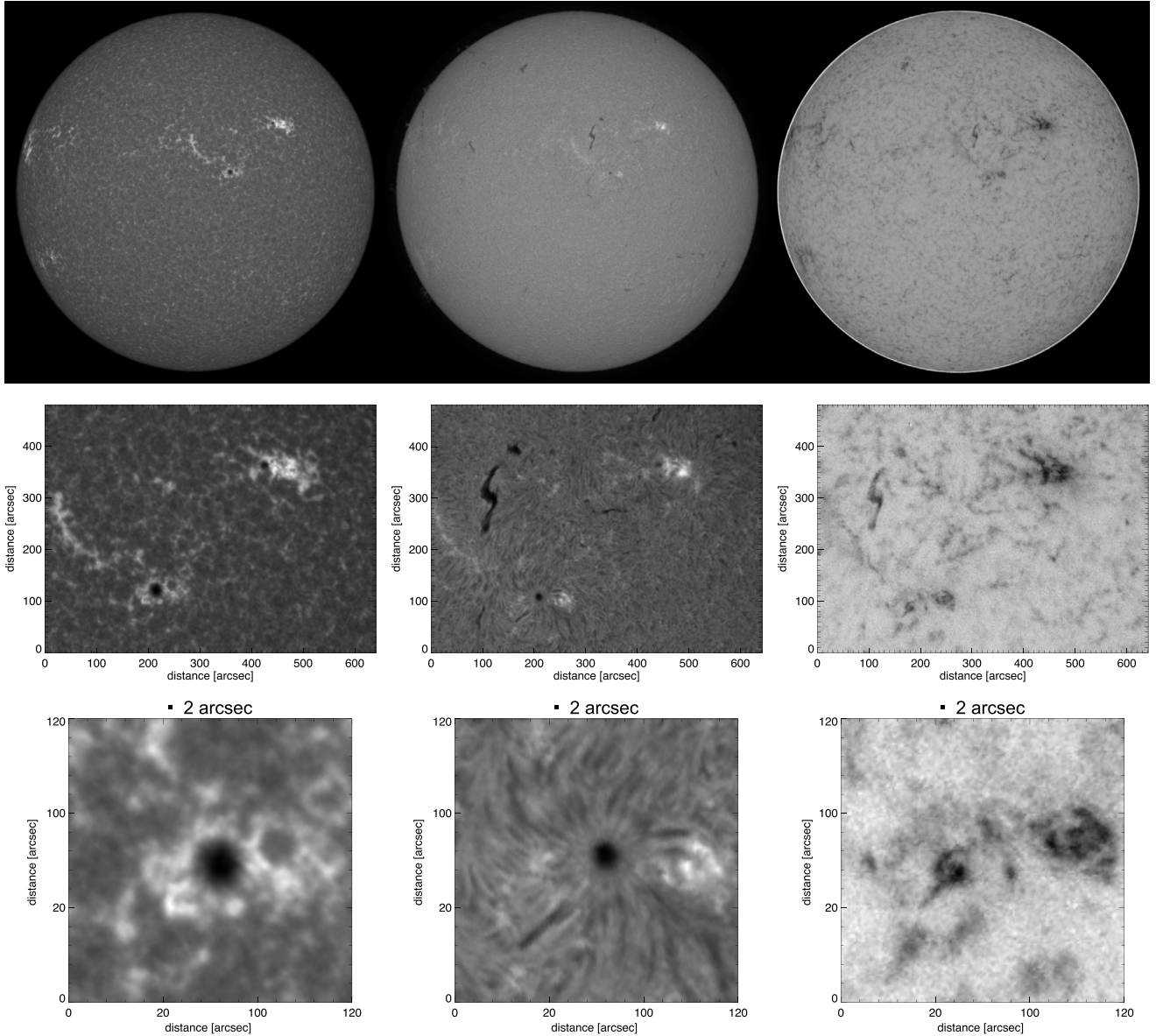
### 5. Line-of-sight velocities in He I 10830 Å

Figure 4 illustrates that a range of  $\pm 3$  Å around the He I triplet is covered by the seven filtergrams. Theoretically, this should enable us to detect LOS velocities of up to about  $\pm 80$  km s<sup>-1</sup>. One possible way to determine the position  $\lambda_{\text{line}}$  of the line in every pixel is a center-of-gravity approach using the filtergram intensities  $I_i$  and the central wavelengths  $\lambda_i$  of the filter passbands known from measurements

$$\lambda_{\text{line}} = \frac{\sum_i (1 - I_i) \lambda_i}{\sum_i (1 - I_i)}. \quad (1)$$

Strong absorption in a filtergram therefore leads to a strong weighting of its central wavelength. Equation (1) is applicable for an undisturbed single spectral line and filtergrams that are normalized to the continuum value. For real data however, a straightforward determination of the line-shift is affected by the influence of other spectral lines, different continuum levels, different line widths and depths, a varying ratio of the blue to red part of the He I triplet, multiple velocity components in a resolution element, and instrumental effects. The theoretical approach described in Eq. (1) therefore has to be extended to account for these (partially unknown) influences. This was addressed by calibrating the line-shift maps generated from the filtergrams with measured line-shift maps from a spectrograph.

In December 2007, parallel observations in He I 10830 Å were made with ChroTel and the Tenerife Infrared Polarimeter (TIP-II, Collados et al. 2007). The TIP-II scans covered three sections of the active region NOAA 10978 on 8 December 2007, each of size 82 × 100 arcsec. The



**Fig. 5.** Sample images from ChroTel on 31 August 2010; full disk and full resolution cutouts. The black squares indicate a size of 2 arcsec in the bottom row. *From left to right:* Ca II K (12:07:39 UTC), H $\alpha$  (10:37:16 UTC), and He I 10830 Å (11:57:17 UTC). An image in the nearby continuum was subtracted from the He I image to enhance the contrast.

stepsize in the scanning direction was 0.5 arcsec; each scan took 15 min (UTC 11:05:28–11:20:58, 11:23:59–11:39:31, 12:03:31–12:19:07). In parallel, ChroTel observations were performed solely in the He I channel with the highest possible cadence of 30 s.

Line-shift maps were compiled from the TIP-II scans by determining the position of the minimum intensity of a smoothed spectrum in the wavelength range between 10828.5 and 10831.9 Å in every pixel, thus between the photospheric Si I line and the water vapor line indicated in Fig. 4. This was done with a precision of one pixel in the spectra, which corresponds to a precision in velocity of  $\sim 300 \text{ m s}^{-1}$ . The maps exhibit a large range of velocities, i.e., blueshifts up to  $-14 \text{ km s}^{-1}$  and redshifts up to  $43 \text{ km s}^{-1}$ .

The regions scanned with TIP-II were cut out from the ChroTel full-disk filtergrams and carefully aligned with the TIP-II maps. To simulate the scanning procedure and the temporal evolution of the observed structures during the scanning

procedure, we first tried to take only stripes from the ChroTel filtergrams closest in time to the actual slit step and to compose an artificial filtergram set from these stripes (cf. Beck et al. 2007, Appendix B). The varying seeing conditions in the ChroTel images however prohibited a reliable composition. We therefore decided to take only the exposure with the best seeing conditions during the 15 min of the TIP-II scan (at UTC 11:15:52, 11:25:15, and 12:07:08). This is justified by the steadiness of most structures seen in the scans, which was verified using movies compiled from the ChroTel images.

To perform a first order correction of the possibly varying influence of the prefilter transmission curve on the measured intensities at different wavelengths, the median filtergram intensities  $\bar{I}_i$  were normalized to the median intensity in the second filtergram. The latter has the least contribution from any spectral line and therefore comes closest to a continuum value. The normalization was done by computing the median value in a centered square covering about 37% of the solar disk in each

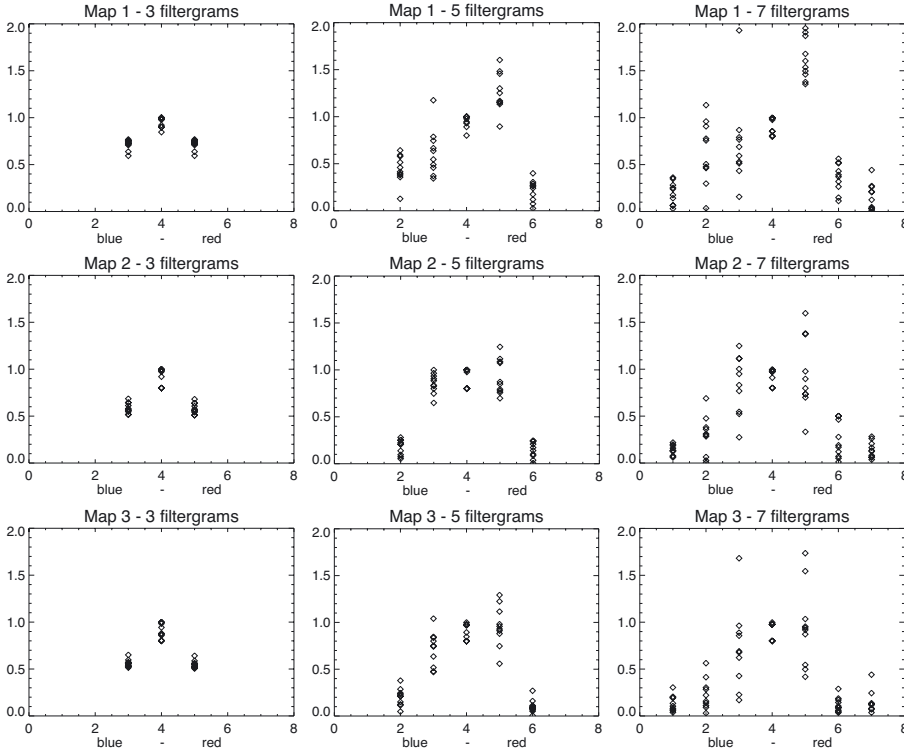


**Fig. 6.**  $\alpha_i$  factors for the reconstruction of the three velocity maps with a different number of used filtergrams. The abscissa denotes the number of the filtergram according to Fig. 4. Each run was repeated ten times to see whether the  $\alpha_i$  converge to a single set (see Sect. 5.2).

filtergram. Each filtergram was subsequently multiplied by the ratio of the median intensity of the second to the actual filtergram

$$\tilde{I}_i = \frac{\bar{I}_2}{I_i} I_i. \quad (2)$$

With the obtained intensities  $\tilde{I}_i$ , the line-shift maps were then computed based on Eq. (1) according to

$$\Delta\lambda_{\text{recon}} = \frac{\sum_i (I_c - \alpha_i \tilde{I}_i) \lambda_i}{\sum_i (I_c - \alpha_i \tilde{I}_i)} - \lambda_0, \quad (3)$$

where  $\lambda_0$  is the rest wavelength of the He I line at 10830.3 Å, and  $I_c$  represents the continuum intensity in every pixel, which was estimated to be

$$I_c = \frac{I_2}{0.95}. \quad (4)$$

The  $\alpha_i$  in Eq. (3) are arbitrary factors that assign an enhanced or decreased weighting to a specific filtergram, hence to a specific wavelength. A variation in these factors thus leads to a different result for the calculated line-shift map. A specific set of  $\alpha_i$  can be considered optimal when the sum over all pixels of the squared difference of the real line-shifts  $\Delta\lambda_{\text{real}}$  computed from the TIP-II scans and the reconstructed line-shifts  $\Delta\lambda_{\text{recon}}$  from the filtergrams is smallest, i.e., when

$$\sum_{\text{pixels}} (\Delta\lambda_{\text{real}} - \Delta\lambda_{\text{recon}})^2 \quad (5)$$

is minimal or

$$\sum_{\text{pixels}} (v_{\text{real}} - v_{\text{recon}})^2 \quad (6)$$

when the line-shifts are expressed as Doppler velocities according to  $v = (\Delta\lambda/\lambda_0) \cdot c$ .

Finding this set of  $\alpha_i$  is an optimization problem that was addressed with the genetic algorithm PIKAIA (Charbonneau 1995). Genetic algorithms are comparably slow, but are known to find global minima more reliably because they employ a random mutation of the fit parameters, which allows them to escape from local minima.

### 5.1. Calibration runs

Calibration runs were conducted with all three TIP-II scans using three, five, and seven filtergrams for the reconstruction. If less than seven filtergrams were used, those that are closest to line center were chosen, e.g., #2–#6 in Fig. 4 for five filtergrams. The runs using a different number of filtergrams were intended to show whether the additional information from the outer filtergrams improves the fit results or might be obsolete.

The values of the  $\alpha_i$  were allowed to vary between 0 and 2. By default, every pixel was treated the same. In additional runs, enhanced weightings were applied to pixels with high absorption depth and to pixels showing small velocities because the latter contribute the largest fraction. Each run was repeated ten times to see whether the results of the optimization algorithm (ideally) converge to a single set of  $\alpha_i$ . The  $\alpha_i$  from the ten runs and from all three maps were then averaged to compile velocity maps for a quantitative analysis.

### 5.2. Convergence of the $\alpha_i$

Figure 6 shows the  $\alpha_i$  parameters for all three calibration maps applying a different number of filtergrams for ten runs each. The distribution of the parameters is consistent for the three maps within a fixed number of used filtergrams. Map 1 shows slightly enhanced weightings of filtergram 5 and decreased weightings of filtergram 3 for the use of five and seven filtergrams, which is

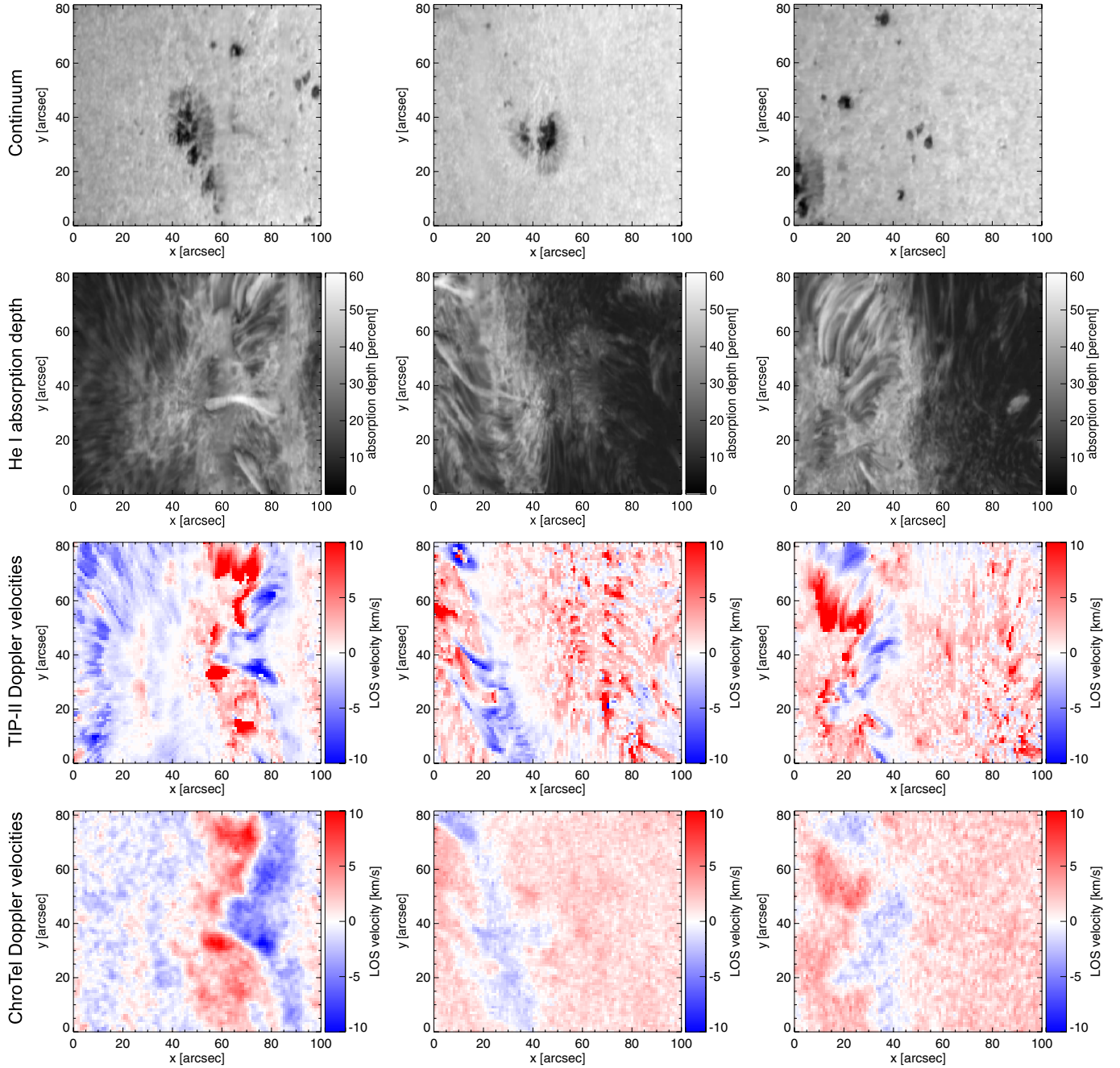


**Fig. 7.** Rows from top to bottom: continuum maps of the three TIP-II scans used for the velocity calibration for ChroTel. He I 10 830 Å absorption depth. He I LOS velocities as determined from the TIP-II spectra. He I LOS velocities as reconstructed from the ChroTel filtergrams (only filtergrams #3–#5; one set of  $\alpha_i$ , same weighting for all pixels. See Sect. 5.1).

because of the high redshifts occurring in this map. For three filtergrams, the code always applies almost the same weighting to filtergram 3 and 5, so the velocities are apparently not reflected in the ratio of  $\alpha_5$  to  $\alpha_3$ , but in the ratio of both  $\alpha_3$  and  $\alpha_5$  to  $\alpha_4$ .

As the number of filtergrams used increases, the spread in the  $\alpha_i$  parameters also increases for the ten runs, indicating that the fits become more arbitrary as the number of fit parameters increases. While the  $\alpha_i$  are mostly confined to within a range of 0.5 for five filtergrams, we find a spread over almost the whole range for seven parameters. This indicates that the application of only three filtergrams seems to be the best choice as long as the velocities are not too large.

### 5.3. Calibration results

The two top rows in Fig. 7 show the absorption depth in He I and the intensity in the nearby continuum of the three TIP-II scans that were used for the velocity calibration. In the third row, the LOS velocities are shown as determined from the TIP-II spectra. For each of these velocity maps, an example of a corresponding velocity map reconstructed from the three innermost ChroTel filtergrams with one set of  $\alpha_i$  is shown for comparison in the lowermost row.

As can be expected from both the lower spatial and spectral resolution, the ChroTel velocity maps lack the fine structures exhibited in the TIP-II maps. This seems to be the case

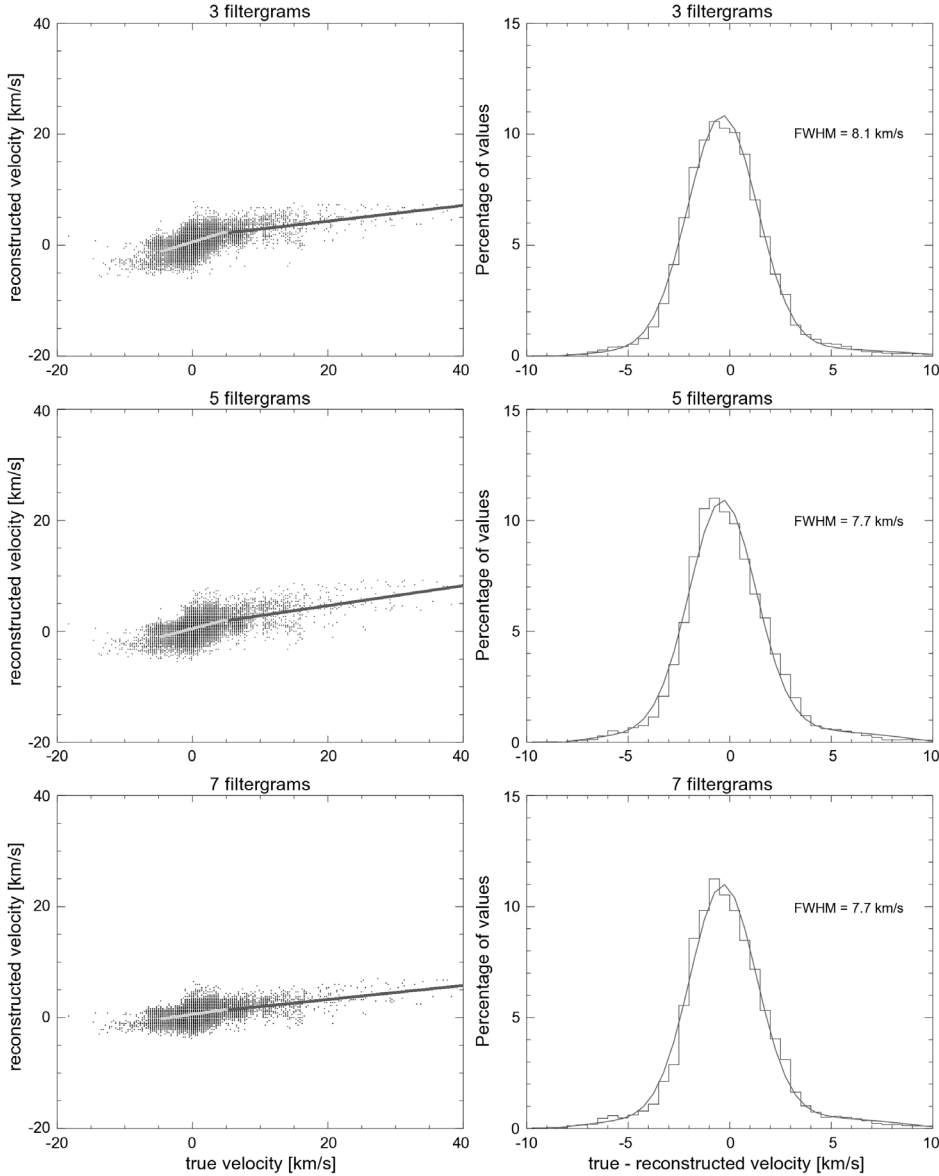


**Fig. 8.** *Left column:* true vs. reconstructed velocities for the use of three, five, and seven filtergrams. The light grey and dark grey lines depict linear-regression fits to the velocity regimes  $-5 < v < 5 \text{ km s}^{-1}$  and  $v \geq 5 \text{ km s}^{-1}$ , respectively. *Right column:* histograms of the velocity difference for the true and reconstructed velocities. The FWHM is calculated from a Gaussian fit to the histograms (see Sect. 5.3.1).

primarily in regions of weak He I absorption, as indicated by the two blueshifted streaks in the second map at about  $x = 15''$ . In contrast to the fine structures on the right-hand side of the map (where the He I absorption is low), the two blueshifted streaks are clearly visible in the ChroTel velocity map, although they are not larger in size. For very low absorption depths, the spectral resolution of the ChroTel filtergrams does not appear to provide the sensitivity to capture the location of the helium-line core accurately, even if it can still be determined in the high-resolution TIP-II spectra.

The overall velocity structure is recovered remarkably well in regions of high absorption depth, although the reconstructed velocities significantly underestimate the real values. This is confirmed in Fig. 8, where the left column shows a scatter plot of the true versus the reconstructed velocities for the use of three, five, and seven filtergrams. While the true velocities reach values of  $40 \text{ km s}^{-1}$  and larger, the values of the reconstructed velocities never exceed  $10 \text{ km s}^{-1}$ .

The scatter plots should ideally display a linear relation over the whole velocity range. We can indeed separate the velocity distribution into two distinct ranges:  $-5 < v < 5 \text{ km s}^{-1}$  and

**Table 3.** Correlation coefficients for the Doppler shift calibration (see Sect. 5.3).

Calibration run	Number of filtergrams	Correlation coefficient	
		$-5 < v < 5 \text{ km s}^{-1}$	$v \geq 5 \text{ km s}^{-1}$
regular	3	0.44	0.47
	5	0.39	0.49
	7	0.30	0.49
small velocities	3	0.44	0.47
	5	0.39	0.49
	7	0.30	0.50
high abs. depth	3	0.44	0.47
	5	0.38	0.49
	7	0.29	0.49

$v \geq 5 \text{ km s}^{-1}$ . For these regimes, the Pearson's correlation coefficient was computed to see how closely the distribution follows a linear relation (cf. Table 3). In addition, histograms of the difference between the true and the reconstructed velocities were computed and fitted with a Gaussian profile (right column in Fig. 8).

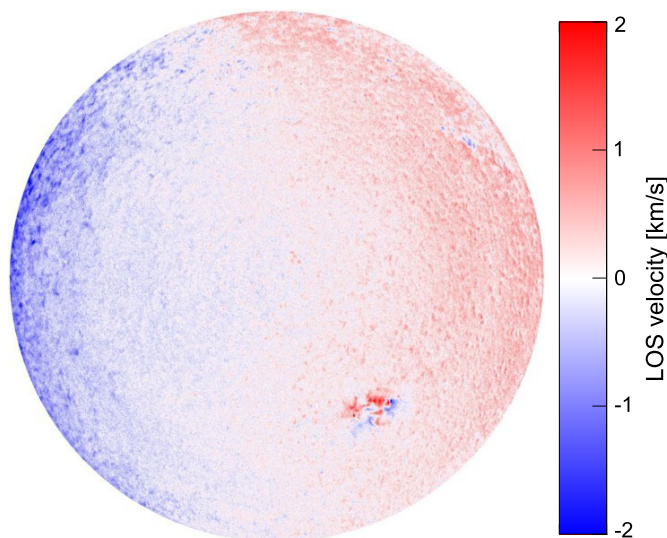


**Fig. 9.** He I LOS velocity for the full disk on 6 July 2009, determined from averaged ChroTel data (UTC 15:58–16:39) using three filtergrams and the mean  $\alpha_i$  parameters from all three calibration maps.

### 5.3.1. Number of filtergrams

The FWHMs of the histograms in Fig. 8 suggest that the calibration gets successively better with the number of filtergrams used. While this seems to be confirmed by the correlation coefficients for redshifts larger than  $5 \text{ km s}^{-1}$ , the opposite is seen for velocities of  $-5 < v < 5 \text{ km s}^{-1}$ . The coefficients drop significantly for seven filtergrams, i.e., the code apparently focusses on the large velocities. Using only the inner three filtergrams therefore seems to be the most effective choice for the reconstruction of velocities up to about  $20 \text{ km s}^{-1}$ . From this point on, the velocities exceed the wavelength coverage of these filtergrams and the outer filtergrams have to be employed.

An FWHM of  $8.1 \text{ km s}^{-1}$  results in  $\sigma = 3.4 \text{ km s}^{-1}$  for the use of three filtergrams. This however does not imply that smaller velocities can not intrinsically be detected. We recall that a lot of fine structure is less likely to be resolved with the lower spatial and spectral resolution of ChroTel, and that we instead observe a “time gradient” in the TIP-II scan, while the ChroTel filtergrams represent a snapshot. In a full-disk Dopplergram (see Fig. 9) created with the mean  $\alpha_i$  from several averaged ChroTel filtergrams, the solar rotation is clearly visible. This means that the accuracy of the LOS velocities must be more precise than  $2 \text{ km s}^{-1}$  for small velocities on large scales.

### 5.3.2. Different weightings

Two additional calibration runs were performed in attempting to improve the precision of the velocity reconstruction. In the first run, only velocities of  $-5 < v < 5 \text{ km s}^{-1}$  were considered for the determination of the  $\alpha_i$  (“small velocities” in Table 3). In the second run, the fit results were weighted with the square of the absorption depth in every pixel (“high abs. depth” in Table 3).

For the first run, the FWHM of the histogram for three filtergrams does not change at all, and the correlation coefficients also vary only very little compared to the regular run where all pixels were treated the same. For the second run focussing on high absorption depths, the FWHM drops insignificantly from  $8.1$  to  $8.0 \text{ km s}^{-1}$ , and again the correlation coefficients display very little variation. The different weightings therefore do not seem to have any significant impact on the calibration quality.

## 6. Discussion and conclusions

The spatial resolution determined in the ChroTel images shows that they are at least comparable in this respect to data from similar instruments such as CHIP for He I, PSPT for Ca II K, or the H $\alpha$  telescope of the Kanzelhöhe Observatory. The main advantage of ChroTel however is the almost simultaneous acquisition of all three spectral lines. Combining this information permits a more accurate estimation of the temperatures and height profiles of structures.

The data are taken with a cadence of three minutes and are also publicly available for long-term *in this cadence*, which is not the case for most other full-disk instruments observing in these lines. Although a cadence up to 30 s would be possible, three minutes were chosen as a compromise between the quantity of data and also trying to catch scarce and short-lived events in the regular mode of observation. The adjustable observing mode nevertheless gives observers the opportunity to take data at a much higher cadence if desired.

The determination of LOS velocities from filtergrams in He I offers an additional tool to study the dynamics of the chromosphere. It has been shown that a precision of at least  $3\text{--}4 \text{ km s}^{-1}$  is possible with the method presented here, i.e., when co-temporal spectrographic maps are available for calibration. Once calibrated, the ChroTel Dopplergrams are a valuable supplement to spectropolarimetric observations because they provide the chromospheric velocity field in the full FOV with a high cadence. This will be demonstrated in a future paper.

The inner five filtergrams seem to be sufficient for creating the Dopplergrams, as the spread of the  $\alpha_i$  and the correlation coefficients for seven filtergrams indicate that the fits become arbitrary. It might be valuable in the future to combine Dopplergrams created with three and more filtergrams to optimize the results over the whole velocity range.

It is unclear to which extent the velocity calibration performed within the scope of this work can be extrapolated and used for regions on the Sun other than the ones considered here. However, that the solar rotation can be detected in full-disk Dopplergrams created with the obtained calibration factors using data from another day provides confidence that these factors might be of a general nature and are not only valid for the specific dataset used for the calibration.

*Acknowledgements.* ChroTel was built and put into operation with the help of many people from the workshops of the participating institutes. Sincere thanks are given to A. Bernert, G. Card, C. Chambellan, H.P. Doerr, R. Friedlein, R. Hammer, T. Hederer, T. Keller, M. Knobloch, A. Lecinski, R. Lull, C. Prah, W. Schmidt, M. Sigwarth, T. Sonner, A. Tritschler, M. Weisschadel, and O. Wiloth. The ChroTel project was funded in part by the Deutsche Forschungsgemeinschaft (DFG).

## References

- Beck, C., Bellot Rubio, L. R., Schlichenmaier, R., & Sutterlin, P. 2007, A&A, 472, 607
- Centeno, R., Trujillo Bueno, J., Uitenbroek, H., & Collados, M. 2008, ApJ, 677, 742
- Charbonneau, P. 1995, ApJS, 101, 309
- Collados, M., Lagg, A., Dıaz Garca, J. J., et al. 2007, in The Physics of Chromospheric Plasmas, ed. P. Heinzel, I. Dorotovic, & R. J. Rutten, ASP Conf. Ser., 368, 611
- Dere, K. P., Bartoe, J., Brueckner, G. E., & Recely, F. 1989, ApJ, 345, L95
- Dupree, A. K., Penn, M. J., & Jones, H. P. 1996, ApJ, 467, L121
- Elmore, D. F., Card, G. L., Chambellan, C. W., et al. 1998, Appl. Opt., 37, 4270
- Ermolli, I., Fofi, M., Bernacchia, C., et al. 1998, Sol. Phys., 177, 1
- Eto, S., Isobe, H., Narukage, N., et al. 2002, PASJ, 54, 481
- Gilbert, H. R., Holzer, T. E., Thompson, B. J., & Burkepile, J. T. 2004, ApJ, 607, 540

- Grossmann-Doerth, U., Schuessler, M., & Steiner, O. 1998, *A&A*, 337, 928
- Habbal, S. R., Woo, R., Fineschi, S., et al. 1997, *ApJ*, 489, L103
- Halbgewachs, C., Bethge, C., Caligari, P., et al. 2008, in *Advanced Software and Control for Astronomy II*, Proc. SPIE, 7019, 70192T
- Harvey, J. W., Hill, F., Hubbard, R. P., et al. 1996, *Science*, 272, 1284
- Kentischer, T. J., Bethge, C., Elmore, D. F., et al. 2008, in *Ground-based and Airborne Instrumentation for Astronomy II*, Proc. SPIE, 7014, 701413
- Krieger, A. S., Timothy, A. F., & Roelof, E. C. 1973, *Sol. Phys.*, 29, 505
- Lagg, A., Woch, J., Solanki, S. K., & Krupp, N. 2007, *A&A*, 462, 1147
- Moreton, G. E., & Ramsey, H. E. 1960, *PASP*, 72, 357
- Neidig, D., Wiborg, P., Confer, M., et al. 1998, in *Synoptic Solar Physics*, ed. K. S. Balasubramaniam, J. Harvey, & D. Rabin, ASP Conf. Ser., 140, 519
- Okamoto, T. J., Nakai, H., Keiyama, A., et al. 2004, *ApJ*, 608, 1124
- Otruba, W. 1999, in *Third Advances in Solar Physics Euroconference: Magnetic Fields and Oscillations*, ed. B. Schmieder, A. Hofmann, & J. Staude, ASP Conf. Ser., 184, 314
- Parker, E. N. 1978, *ApJ*, 221, 368
- Peter, H. 1999, *ApJ*, 516, 490
- Peter, H., & Judge, P. G. 1999, *ApJ*, 522, 1148
- Phillips, J. L., Bame, S. J., Feldman, W. C., et al. 1995, *Adv. Space Res.*, 16, 85
- Rüedi, I., Solanki, S. K., & Livingston, W. C. 1995, *A&A*, 293, 252
- Scherrer, P. H., Bogart, R. S., Bush, R. I., et al. 1995, *Sol. Phys.*, 162, 129
- Schmidt, W., Muglach, K., & Knölker, M. 2000, *ApJ*, 544, 567
- Steinberger, M., Denker, C., Goode, P. R., et al. 2000, in *The Solar Cycle and Terrestrial Climate, Solar and Space weather*, ed. A. Wilson, ESA SP, 463, 617
- Thompson, B. J., Plunkett, S. P., Gurman, J. B., et al. 1998, *Geophys. Res. Lett.*, 25, 2465
- Thompson, B. J., Reynolds, B., Aurass, H., et al. 2000, *Sol. Phys.*, 193, 161
- Trujillo Bueno, J., Merenda, L., Centeno, R., Collados, M., & Landi Degl'Innocenti, E. 2005, *ApJ*, 619, L191
- Tu, C., Zhou, C., Marsch, E., et al. 2005, *Science*, 308, 519
- Vršnak, B., Warmuth, A., Brajša, R., & Hanslmeier, A. 2002, *A&A*, 394, 299
- Warmuth, A., Vršnak, B., Aurass, H., & Hanslmeier, A. 2002, in *Solspa 2001, Proceedings of the Second Solar Cycle and Space Weather Euroconference*, ed. H. Sawaya-Lacoste, ESA SP, 477, 195
- Wilhelm, K., Curdt, W., Marsch, E., et al. 1995, *Sol. Phys.*, 162, 189